Kaolinite structural modifications induced by mechanical activation

Jofre Mañosa[a], Jaume Calvo-de la Rosa[b], Alessio Silvello[c], Alex Maldonado-Alameda[a], Josep Maria Chimenos[a, *]

[a] Departament de Ciència de Materials i Química Física, Universitat de Barcelona, C/ Martí i Franquès 1, 08028, Barcelona, Spain

[b] Departament de Física de la Matèria Condensada, Facultat de Física, Universitat de Barcelona, C/ Martí i Franquès 1, 08028 Barcelona, Spain.

[c] Thermal Spray Center CPT, Universitat de Barcelona, Barcelona, Spain.

* Corresponding author e-mail: chimenos@ub.edu

Abstract

This study presents novel characterisation techniques to evaluate the effects of mechanical activation (MA) on the kaolinite structure. MA was achieved with a planetary ball mill at various times and rotation speeds to get different activation degrees. A thermal activation was performed for comparison purposes. The results of X-ray diffraction and selective area electron diffraction demonstrated that the kaolinite content was significantly reduced as the amorphous phase increased. Illite, K-feldspars, and quartz impurities were extensively modified as well. The morphology of kaolinite particles is altered. Furthermore, the mechanical treatments significantly affected the hydroxyls, losing bonding strength with the structure, as stated with ^{1}H nuclear magnetic resonance. Thermogravimetric analysis and infrared spectroscopy also revealed that water molecules could be formed due to the reaction of hydroxyls between them or with the atmosphere. This work improves the comprehension of MA on kaolin by clearly confirming with new techniques that the mechanical treatments distort the kaolinite structure.

Keywords: Mechanical activation; Kaolin; Dehydroxylation; Kaolinite; Metakaolin

1. Introduction

Clays are some of the most used materials in the industry, and among them, kaolin rises as one of the most important (Khalifa et al., 2020). This is the most mined clay used in a wide variety of sectors, such as the construction industry, catalysis, paper industry, and ceramic industry, among others (Efavi et al., 2012; Zhao et al., 2021; Richard and Rendtorff, 2022). Kaolin is a clay mainly composed of kaolinite, $Al_2Si_2O_5(OH)_4$, which is a 1:1 layered clay mineral, where each layer (~7 Å thickness) comprises a tetrahedral sheet (SiO_4) and an octahedral sheet ($Al(O,OH)_6$) (Sperinck et al., 2011; Vaculíková et al., 2011; Wang et al., 2011). Tetrahedral and octahedral sheets are strongly bonded through covalent bonds by sharing a common plane of oxygens and hydroxyls (Maier et al., 2021). The layers are bonded through weak hydrogen bonds formed with the hydroxyls from Al octahedra and oxygens of Si tetrahedra from the adjacent layer (Johnston et al., 2008). Kaolin usually has impurities such as other clay minerals (illite, muscovite), quartz and feldspars, among others, changing some of the properties of the mineral. Due to the well-packed structure of kaolinite, the layers are difficult to move or break, making kaolin the least reactive clay (Miranda-Trevino and Coles, 2003). Therefore, for some applications such as for the construction industry, they must be previously activated (Cao et al., 2021; Mañosa et al., 2021). Due to their function of forming hydrogen bonds between layers, the hydroxyl groups play a crucial role in achieving kaolin's activation.

The most common treatment to increase the kaolin reactivity is by thermal activation (TA), involving the dehydroxylation of clay. Through thermal energy, the hydroxyls are removed from the structure at temperatures between 500-900 ℃ depending on the clay type and their characteristics (e.g., purity, substitutions, etc.), while overheating leads to the formation of inactive crystalline phases (Izadifar et al., 2020). TA of kaolinite causes a change in the octahedral AlO_6 sheet due to the loss of OH groups, decreasing the Al coordination from VI to V and IV, while the tetrahedral SiO_4 sheet is mainly retained (Osornio-Rubio et al., 2016; Peng et al., 2018). Furthermore, the hydrogen bonds between layers are also removed due to the transfer of hydroxyl groups to the surroundings, causing

the material's amorphization. The material obtained from the kaolinite dehydroxylation is known as metakaolinite ($Al_2Si_2O_7$), which is much more reactive and valuable for some applications (Ptáček et al., 2014). However, due to the high energy consumption of thermal processes, mechanical activation (MA) has recently emerged as a feasible clay activation method.

Mechanical (mechanochemical) treatments strongly modify the characteristics of raw clay. There is a large availability of devices which are moderately priced, such as rolling mills, mixer mills or planetary mills among others, that are suitable for laboratory-scale mechanical activation or even industrial applications (Kása et al., 2021). Thus, various clay minerals, milling parameters and applications of mechanically activated clays have recently been studied (Rudmin et al., 2020; Georgopoulos et al., 2021; Pálková et al., 2021; Kása et al., 2022). MA causes the destruction of the crystal structure by breaking chemical bonds, therefore obtaining a highly amorphous material (Hamzaoui et al., 2015). The obtained mechanically activated kaolin is therefore more reactive since its reactivity is related to its structural order (Valášková et al., 2011; Baláž et al., 2013). MA has some advantages and disadvantages compared to TA. For instance, MA is less energetic than TA, with a reduction of around 200-1000 kWh per ton of mechanically activated kaolin produced in front of metakaolin (~1600 kWh/t) (Fitos et al., 2015). However, previous studies have demonstrated that this material has some drawbacks compared to metakaolin. Not all aluminium is V- or IV-coordinated (Mañosa et al., 2022), and prolonged milling times promote the formation of agglomerates, reducing the specific surface area and increasing the mean particle size (Valášková et al., 2011). Furthermore, there is a lack of knowledge about the changes induced in hydroxyls and their surroundings. Some theories have been presented, such as the formation of water molecules.

This work is the extension of a previous work where the reactivity of mechanically activated kaolin was evaluated (Mañosa et al., 2022). In this research, the authors present new results focused on the microstructural variations of mechanically activated kaolin that could improve the comprehension of this material. To facilitate a better understanding, this study is divided into two main parts; the first

78 part is a structural analysis using novel techniques, such as the reference intensity ratio method using

79 X-ray diffraction (RIR-XRD), to easily monitor the effect of MA on not only kaolinite but also some

80 common impurities contained in kaolin, and transmission electron microscopy (TEM) to study both

81 the particle aggregation and the sample crystallinity through electron diffraction. The second part

82 focuses on the OH surroundings' alterations, which is still a controversial topic. This study combined

83 conventional characterisation methods, such as Fourier transform infrared spectroscopy (FTIR) and

84 thermogravimetric analysis (TGA), and proton nuclear magnetic resonance (^{1}H NMR), allowing a

85 deeper understanding of the alterations in this part of the kaolinite structure.

2. Materials and Methods

2.1 Materials and activation methodology

88 The raw kaolin (K) was provided by Minerals i Derivats, S.A. (Spain). The chemical composition

89 of K, measured through X-ray fluorescence (XRF) with a Panalytical Philips PW 2400 sequential X-

90 ray spectrophotometer, is shown in Table 1. The main crystalline phases were kaolinite (~82-92 wt.%),

91 quartz (~6-12 wt.%), illite (~2-7 wt.%) and potassium feldspar (K-feldspar) (~1-5 wt.%). MA and TA

92 were performed in parallel on raw kaolin to obtain comparative results following the methodology of

93 previous work (Mañosa et al., 2022). Briefly, TA (thermal dehydroxylation) was performed in a

94 laboratory oven at 750 ºC for 6 h to obtain a reference metakaolin (MK) while MA was performed in

95 a planetary ball mill PM 400 (RETSCH) equipped with 125 mL zirconia jars and 10 mm zirconia balls.

96 20% of the volume was occupied with the sample and balls, maintaining a balls-to-sample mass ratio

97 of 20. The mechanical treatments were conducted at 250, 300 and 350 rpm for 30, 60 and 120 min,

98 obtaining 9 combinations. For comparison purposes in some tests, an additional mechanical treatment

99 has been performed at 250 rpm for 15 min. The nomenclature of the samples through this work is KS-

100 T, with S as the rotation speed and T as the milling time.

Table 1. The chemical composition of the raw kaolin.

Oxide	Mass %
SiO_2	49.85
Al_2O_3	36.31
K_2O	0.69
Fe_2O_3	0.47
CaO	0.16
TiO_2	0.15
Na_2O	0.13
MgO	0.11
P_2O_5	0.08
LOI	12.03

102

103   2.2 Characterisation

104   2.2.1 Structural characterisation

105   X-ray powder diffraction (XRD) was used to determine the crystalline phases with a Bragg-

106   Brentano PANalytical X'Pert PRO MPD alpha1 (CuKα_1, λ=1.5406 Å) powder diffractometer. Five

107   repeated scans were performed with a measuring time of 100 s and a step size of 0.026º. A focalising

108   primary monochromator (Ge (111)), an anti-scatter slit (4º) and a Soller slit (0.04 rad), were used for

109   the measurements. The high degree of overlapping between reflections and the low signal-to-noise

110   ratio (SNR) between XRD reflections and background complicate the capacity to perform a reliable

111   Rietveld refinement to the experimental data. To solve that issue and provide the most accurate

112   qualitative and quantitative analysis, we processed the data from the most relevant XRD reflections

113   which are not overlapped with other reflections by two different methodologies:

114   (i)   By measuring the area and width through a self-made Python® code which makes a profile

115   fitting of the experimental data to a pseudo-Voigt function, $pV(2\theta)$, defined by:

116
$$pV(2\theta) = \eta L(2\theta) + (1 - \eta)G(2\theta)$$

being $L(2\theta)$ and $G(2\theta)$ the Lorentzian and Gaussian components respectively, while η refers to the Lorentzian factor (i.e., sets which is the relative degree of Lorentzian or Gaussian behaviour of the reflection). 2θ denotes the angular position in the diffractogram.

From the $pV(2\theta)$ fitting process one may quantify the reflections area (h), width (by means of full width at half maximum, β), as well as the Lorentzian factor (η). Each reflection's β value can be used to approximate the crystallite size (τ) using the Scherrer equation:

$$\tau = \frac{K\,\lambda}{\beta\,\cos\theta}$$

where λ refers to the radiation wavelength (in our case, $\lambda = 0.145$ nm) and K is a geometrical constant (we use $K = 0.94$). The effective sample effect on β was obtained after removing the instrumental contribution, which was obtained by measuring a LaB_6 pattern and fitting the obtained data to a Cagliotti function.

(ii)   By doing the same XRD reflection fitting but with the commercial TOPAS® software. In this case, the software provides an estimation of the area and τ, using the fundamental parameter approach function, which subtracts the equipment contribution to the reflection width, using a calibration. The same LaB_6 pattern was used in both methods as calibration data. The areas and τ obtained through TOPAS were compared with the ones obtained from Python.

Therefore, we faced the problem of measuring the reflections' relative area and width (which are directly related, respectively, to each phase relative quantity and crystallite size) with two different approaches, in order to check the robustness of our results. The most significant reflections, in terms of high SNR and non-overlapping with neighbouring reflections, are those listed in Table 2. These are the reflections that were used for the Python and TOPAS analyses.

139 Table 2. XRD reflections analysed. 2θ angle (°) represents the centre of the reflection, while 2θ range

140   (°) refers to the region at each side of the reflection centre given to the algorithm to perform the

141   computation.

	2θ angle (°)	2θ range (°)
Kaolinite	12.4	± 2.0
Quartz	26.6	± 1.2
	50.0	± 0.7
K-feldspar	27.5	± 0.4

142

143   Scanning electron microscopy (SEM) was used to evaluate the microstructure of the powder. For

144 this purpose, the samples were coated with carbon and analysed with a JEOL J-7001F microscope

145 operated at an accelerating voltage of 15 kV. Furthermore, TEM was also used to evaluate the particle

146 morphology before and after the treatments. For this technique, the samples were previously dispersed

147 in ethanol, sonicated to minimise agglomeration, and deposited on copper grids. TEM images and

148 diffraction patterns were acquired in a JEOL J2010F microscope operated at an accelerating voltage

149 of 200 kV, equipped with a FEG electron gun, and coupled to a Gatan ORIUS CCD camera. In

150 addition, selective area electron diffraction (SAED) was used to confirm the crystallinity variations

151 observed through XRD.

152   2.2.2 OH groups alterations

153   A Spectrum Two™ Perkin Elmer spectrometer in attenuated total reflectance (ATR) mode in the

154 range 4000–450 cm^{-1}, with a resolution of 4 cm^{-1} and 32 scans for the analysis of 4000-3000 cm^{-1} and

155 1800-1500 cm^{-1} regions was used for the study of the hydroxyls' modifications. The ATR method was

156 selected to avoid interferences due to air humidity, and KBr hydration is often observed using

157 transmission mode FTIR devices. TGA was accomplished using an SDT Q600 device (TA

158 Instruments), with a heating rate of 10 ºC/min up to 1200 ºC in a synthetic air atmosphere (50 mL/min).

159 ^{1}H magic angle spinning nuclear magnetic resonance (MAS NMR) spectra were recorded at room

temperature in an AVANCEIII HD 600 (Bruker AXS) spectrometer using a triple resonance DVT probe of 2.5 mm at a spinning rate of 25 kHz. The magnetic field was 14.1 T, corresponding to a ^{1}H resonance frequency of 600.09 MHz. The ^{1}H-NMR chemical shifts are referenced to Glycine. ^{1}H MAS NMR spectra were recorded with a 2-us 90º pulse and 3-s delay (^{1}H Single pulse) and summing up 64 scans.

## 3. Results and discussion

3.1 Structural characterisation

The X-ray powder diffractograms of K, MK and mechanically activated samples are shown in Fig. 1a to evaluate the effect of mechanical treatments with several degrees of intensity in the crystalline phases, while Fig. 1 b,c,d present selected representative samples in various regions of the diffractograms. The main crystalline phases detected in K were kaolinite (Kaol) and quartz (Q), while some reflections of illite (I) and K-feldspar (F) were also observed. With MA the crystallinity of the samples decreases (less intense reflections of kaolinite mainly), obtaining a diffractogram similar to MK in the most energetic mechanical treatments. The effect of MA and TA on the kaolinite and illite structures can be well studied in Fig. 1b. The (002) illite reflection was almost indiscernible for any MA sample; therefore, it can be assumed that illite is completely amorphized during the MA process. In contrast, the slight illite reflection shift in MK suggests a change in its unit-cell parameter caused by dehydroxylation (Sánchez-Soto et al., 2007; Wang et al., 2017). Kaolinite is not fully amorphized during the weakest mechanical treatments (exemplified with K250-30). The decrease of intensity in the (001) reflection (basal reflection) suggests that through MA the hydrogen bonds between kaolinite layers are broken, drastically affecting the stacking in kaolinite (Frost et al., 2001). By increasing the milling time and the rotation speed, the intensity of the reflection corresponding to the kaolinite's (001) reflection diminishes (K300-60) until disappearing in the most activated samples (represented by K350-120), likely meaning that the long-range ordering in the layers is also disturbed and an

184 amorphous phase is obtained. However, it is remarkable how the intensity of all kaolinite's reflections

185 is substantially reduced even with the less aggressive treatments. In addition to the abovementioned

186 lattice modification, the observed reflection broadening reveals that the crystallite size decreases

187 during the MA as well.

188   The kaolinite and illite amorphization is associated with the appearance of a halo centred at around

189 25 and 30° 2θ angles, corresponding to the amorphous material (Derouiche and Baklouti, 2021). Fig.

190 1c presents the diffractograms focusing on the amorphous halo. The reduced kaolinite-related

191 reflections could be directly associated with the amorphous phase formation. In K250-30, there was

192 less contribution of amorphous content than in the more activated samples since the kaolinite

193 reflections were also more intense. This fact is due to a disorder of kaolinite, mainly in the layer

194 stacking, but not a total transformation to the amorphous phase. Therefore, the sample K250-30 could

195 be referred to as poorly ordered kaolin. K300-60 presented a significant amorphous content, but some

196 kaolinite contribution was still observed, while K350-120 presented the highest amorphous halo and

197 absence of kaolinite reflections. Kaolinite reflections were also unseen in MK, and a remarkable

198 amorphous halo was also observed. In Fig. 1c, the other crystalline phases of the samples, i.e. quartz

199 and K-feldspar, can also be observed. Both Q and F were apparently unaffected by thermal and low

200 energetic mechanical treatments. However, a significant decrease in F reflection was detected with the

201 most aggressive mechanical treatment (K350-120).

202   The effect of MA in quartz is detailed in Fig. 1d, showing a significant decrease in the intensity of

203 the quartz (011) reflection in K350-120, accompanied by a broadening of the reflection. This

204 broadening is likely due to quartz's crystallite size reduction during highly energetic MA (Marinoni

205 and Broekmans, 2013; Derouiche and Baklouti, 2021). Some quartz could even be amorphized due to

206 the process of radical generation, which takes place with very high energetic mechanochemical

207 treatments, where amorphous and reactive Q^2, Q^3 and/or Q^4 Si environments are formed (Gobindlal et

208 al., 2021). Quartz remained unaltered in the samples with less vigorous mechanical treatments,

209 although in K300-60, a slight intensity reduction and reflection broadening could be perceived. The

210 hardness of the crystalline phases plays a crucial role in the amorphization of the material through MA

211 (Makó et al., 2001; Tole et al., 2018). Illite was the first to be amorphized (Mohs hardness 1-2),

212 simultaneously with kaolinite (Mohs hardness 2-3). K-feldspar (Mohs hardness 6-6.5) and quartz

213 (Mohs hardness 7) were modified only with the most energetic mechanical treatments with probably

214 some amorphization.
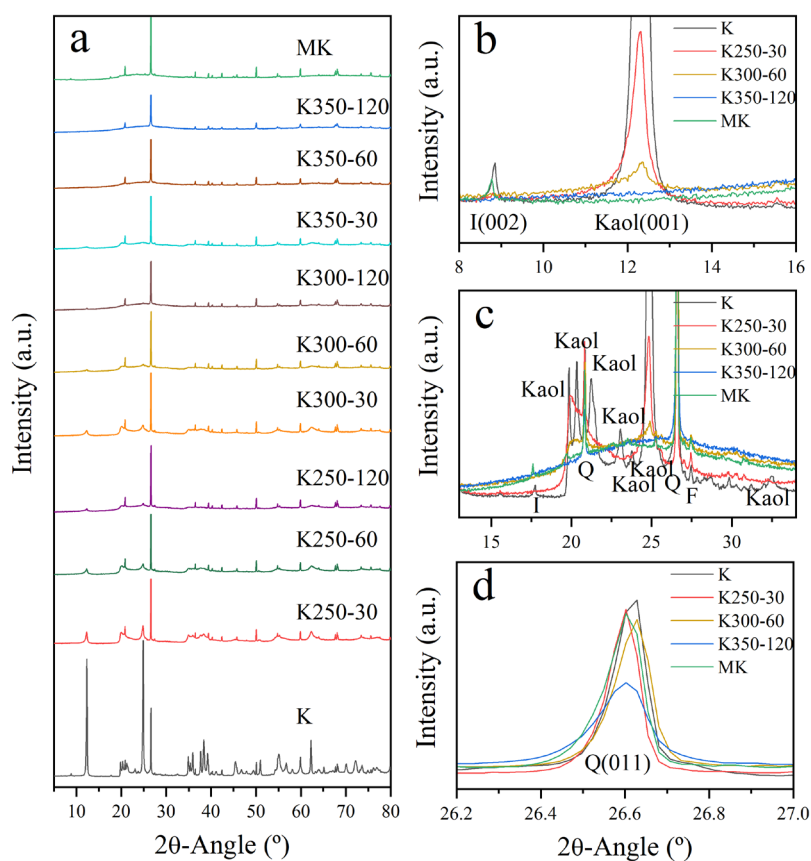
Fig. 1. X-ray powder diffractograms at the 2θº regions between (a) 5-80°, (b) 8-16°, (c) 14-34º and (d) 26.2-27.0º for K, K250-30, K300-60, K350-120 and MK. I=illite, Kaol=kaolinite, Q=quartz, F=K-feldspar.

219 The crystallographic modifications produced by the MA mechanism were analysed by studying the

220 variation in the reflections' characteristics as a function of the experimental conditions. As described

221 in Section 2, this evaluation was performed both with Python and TOPAS. As clear proof of the

222 dependence between the sample's microstructure and the MA conditions, we provide in Fig. 2 a

summary of the appearance of one of the reflections of each of the phases for three representative

conditions of the MA used (K250-30, K300-60 and K350-120). This summary provides some starting

clear evidence. First, illite's reflections are very weak and only detected for the least severe MA

conditions. The low SNR present even when the reflection is observable makes it impossible to

perform a profile fitting with the required reliability. Nonetheless, these results show up that the initial

samples contained a low fraction of illite, which disappeared as the MA process started. On the other

hand, we have good resolution reflections for the kaolinite, quartz, and K-feldspar phases, which can

be studied in greater detail. One must also pay attention to the fact that the intensity of the reflections

decreased in all cases, meaning that the content of the crystalline phases was reduced due to the MA

process. This is in very good agreement with the amorphization arguments presented before. In this

same direction, it is important to highlight that this decrease in the reflections' intensity difficulted the

profile fitting process for the most severe MA conditions in kaolinite and K-feldspar when the

reflection's intensity was comparable with the background noise one.
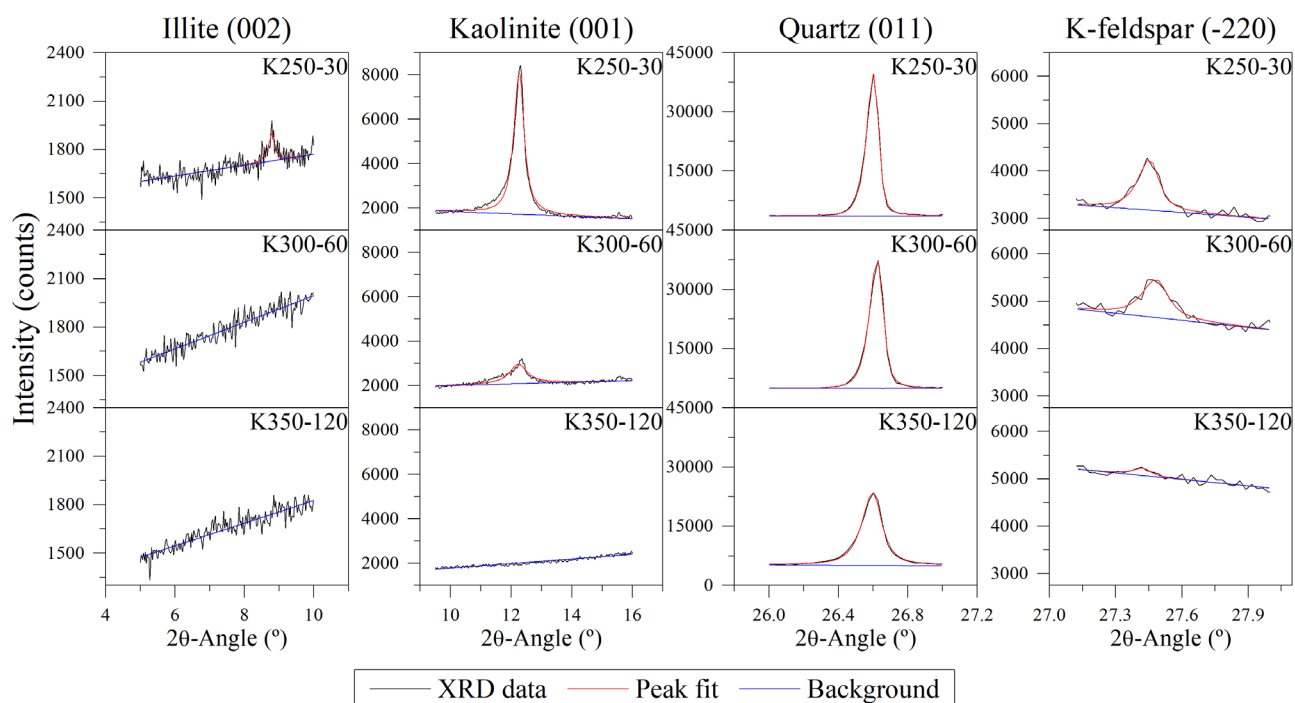
Fig. 2. Fitting of illite (002), kaolinite (001), quartz (011), and K-feldspar (-220) reflections after MA
for K250-30, K300-60, and K350-120.

As described in detail in Section 2, we have taken the experimental data of some of the clearest reflections of the kaolinite, quartz and K-feldspar phases and used a Python script and TOPAS software to quantify the change in the relative area and width of each reflection as a function of the MA conditions. Despite we were not capable to obtain an exact quantification of the relative content between phases as done by the Rietveld method, this analysis is capable to provide a reliable quantification of the crystallographic changes produced to each phase as a function of the MA, given that all samples were prepared and measured under the same conditions.

Fig. 3 depicts the results obtained from measuring the reflections area (A_r) with Python, by the $pV(2\theta)$ profile fitting, and by TOPAS, which is directly related to the relative amount of each phase. The results provide different conclusions of interest. The first one is the perfect match between the results extracted by the two methods in all cases. This is an excellent symptom of the robustness and precision of the methods used. Secondly, in good agreement with the qualitative observations made in Fig. 1, there is in fact a reduction of the reflections areas for all phases as the MA process becomes more intense. This dependence is fulfilled both as a function of the milling time (all curves have negative slope) and milling speed (the decrease is always greater at 350 rpm than at 300 rpm and 250 rpm). The phase that suffered the most significant reduction when the MA process started was kaolinite. As an example, there is a 80% of intensity reduction even in the K250-30 case, showing that the kaolinite phase quickly disappears when MA starts. On the other hand, the presence of quartz and K-feldspar was also reduced but at a lower rate. In these two cases, the MA at 250 rpm was not reducing the amount of phase present, but 300 or 350 rpm was required to produce changes. The slight percentage increases at low rotation speed and milling time are due to the fitting process and the difficulty to fit a reflection with very low intensity, especially in the case of K-feldspar (see Fig. 2) where the measurement error is also higher. Overall, the strongest conditions lead to residual quantities of kaolinite, around 85% of the initial amount of quartz and 25% in the case of K-feldspar. These numerical results are again in excellent agreement with the observations in Fig. 1.
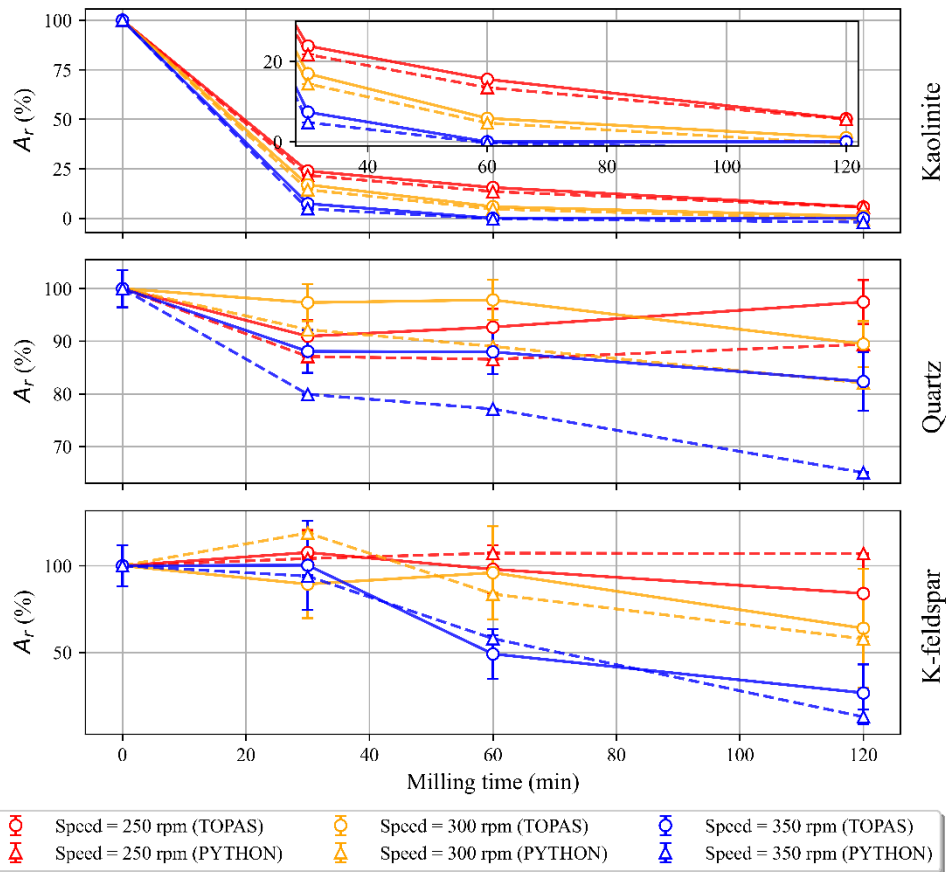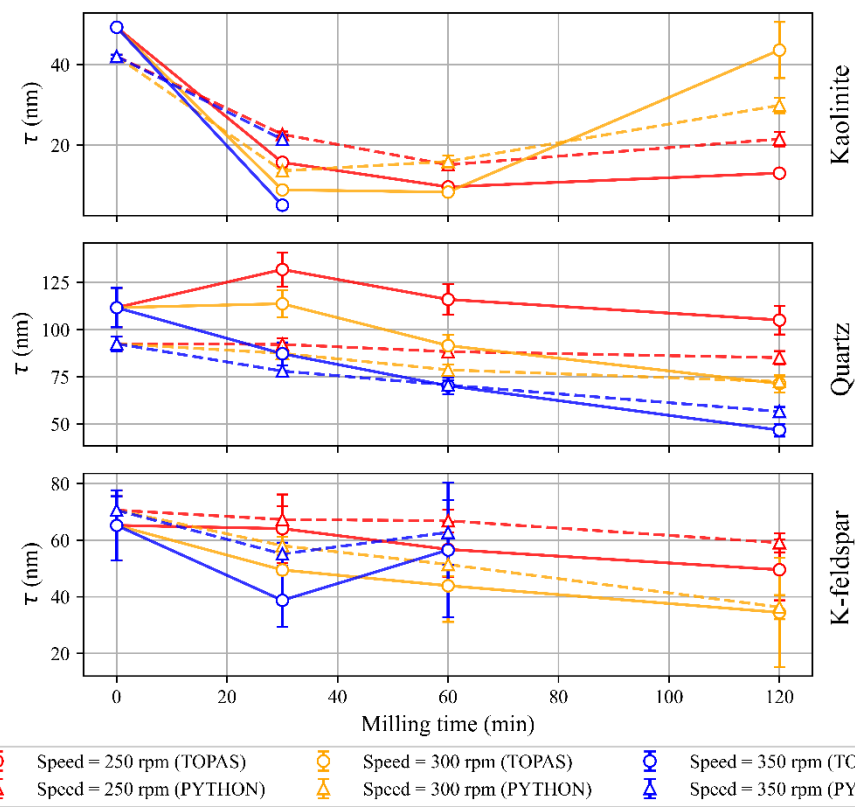
Fig. 3. Dependence of the measured relative reflection area (A_r) with the MA conditions. The top figure shows the results for the kaolinite reflection at 12.4° (d=0.71 nm), the middle one corresponds to the mean values for the quartz's reflections at 26.6° (d=0.34 nm) and 50.0° (d=0.18 nm), and the bottom corresponds to the K-feldspar reflection at 27.5° (d=0.32 nm). Circular points and solid lines correspond to the area measurements from the Python fit, while the triangular points and dashed lines refer to the results obtained by the TOPAS fitting.

Once the concentration monitoring has been done, we study now how the MA might affect the crystallite size of each phase. Each reflection width was measured by fitting the experimental data to a $pV(2\theta)$ function with Python and TOPAS. The obtained results are presented in Fig. 4. The missing points were removed due to the impossibility to achieve a good fit with the low SNR. The top plot in Fig. 4 shows that the MA process quickly reduced the crystallite size of the kaolinite phase, which might be attributed to the mechanical fracture of the crystals. The size then remained stable around 10 – 20 nm. The K300-120 data (both from Python and TOPAS fitting) shows a slight increase in the

278 crystallite size. Considering the conditions where this phenomenon appears, these observations open

279 the possibility of having mechanical alloying of kaolinite crystals for long and high-speed MA

280 processes. For quartz the tendency is more stable, so the MA process seems to be reducing gradually

281 its crystallite size, although for 250 rpm treatments the crystallite sizes were practically unaffected.

282 Finally, the MA gradually reduced the crystallite size of K-feldspar for 250 rpm and 300 rpm processes,

283 but again a change of tendency for the most energetic process was detected. Therefore, we may

284 conclude that the MA process initially reduces the crystallite size of all phases, but mechanical alloying

285 cannot be discarded for highly energetic conditions according to our observations.

287 Fig. 4. Dependence of the measured crystallite size (τ) with the MA conditions. The top figure shows

288 the results for the kaolinite reflection at 12.4° (d=0.71 nm), the middle one corresponds to the mean

289 values for the quartz's reflections at 26.6° (d=0.34 nm) and 50.0° (d=0.18 nm), and the bottom

290 corresponds to the K-feldspar reflection at 27.5° (d=0.32 nm). Circular points and solid lines

291 correspond to the crystallite size measurements by TOPAS, while the triangular points and dashed

292 lines refer to the results obtained with Python. Kaolinite's results from K350-60 and K350-120

293   samples, and from K-feldspar's K350-120 samples have not been considered due to the lack of

294   precision in the β measurements due to the low SNR at these conditions.

295   Fig. 5 presents SEM (a-d) and TEM (e-h) images of K, MK, and low and high-energy mechanically

296 activated samples. K presented mainly hexagonal kaolinite particles (Fig. 5e), which were stacked

297 forming books (Fig. 5a) (San Cristóbal et al., 2010). The particles present the kaolinite's characteristic

298 shape with sharp edges (N'Guessan et al., 2021). After TA, in SEM images (Fig. 5d), the kaolinite

299 particles presented the same morphology, meaning that although dehydroxylation causes a significant

300 distortion in the kaolinite structure, the morphology is barely affected (De Souza Santos et al., 2005).

301 However, slightly rounded corners could be observed in TEM images (Fig. 5e). In contrast, the MA

302 causes a total disruption of the particles' morphology. In Fig. 5b,c, a significant particle size reduction

303 was detected. However, MA causes the formation of particle aggregates through chemical bonds,

304 which could also be observed. Therefore, although the particle size is reduced, these agglomerates

305 could cause an increase in the particle size distribution and a reduction of the specific surface area

306 (Balczár et al., 2016). The variation in the morphology was also well observed in TEM images (Fig.

307 5f,g). The hexagonal crystals previously observed were modified to particles with irregular sizes and

308 shapes.

309
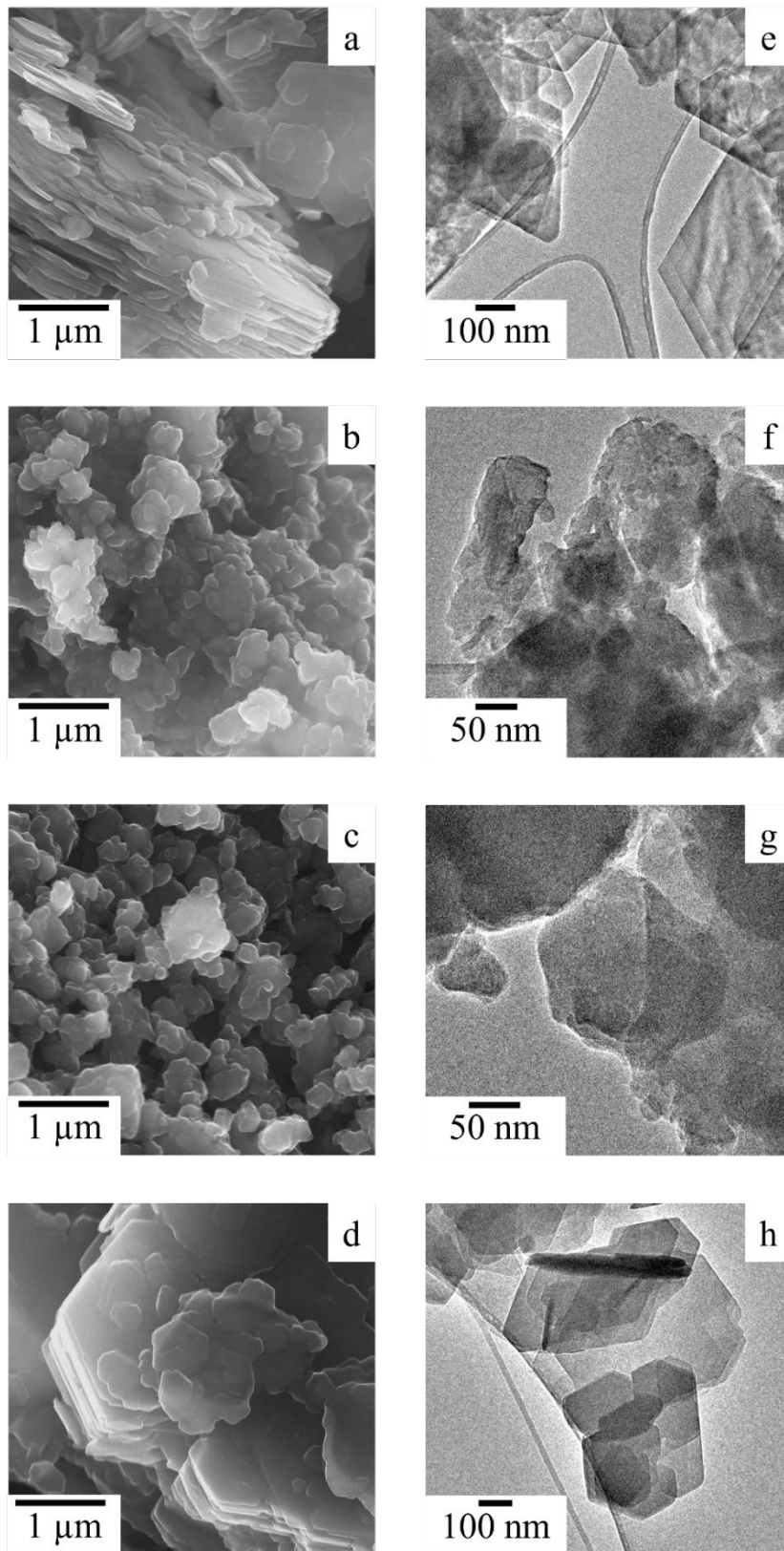
Fig. 5. Electron microscopy images (a-d) SEM and (e-h) TEM for (a, e) K, (b, f) K250-30, (c, g) K350-120, and (d, h) MK.

312   Fig. 6 depicts representative selective area electron diffractions (SAED) of each sample obtained

313   through TEM. K presented a high degree of crystallinity, with its characteristic triclinic hexahedral

314   diffraction pattern (Xu and Van Deventer, 2002). Fig. 6a presents the SAED of two or more kaolinite

315   crystals with a high degree of crystallinity. However, there were some regions where a diffuse ring

316   could probably be detected, meaning there was also some slight contribution of the amorphous phase

317   (Fig. 6a upper corner). Similar behaviour was observed in K250-30, although the material was already

318   relatively amorphous in this case. Here the crystalline pattern was practically indiscernible, meaning

319   that the kaolinite structure was already highly modified and probably semicrystalline (Xu and Van

320   Deventer, 2002). The number of detected reflections was lower than in previous samples, and the spots

321   became broad. In the more amorphous regions (Fig. 6b upper corner), a majority of the diffuse halo

322   was detected while some minor crystallinity was still observed, some of them starting to form rings.

323   With intense MA (K350-120, Fig. 6c), the amorphous phase was predominant, confirming the results

324   observed through XRD, while some spots corresponding to crystalline material were detected in some

325   patterns. At least three diffuse rings were detected with the intensity profile of the pattern. The d-

326   spacings of the rings were approximately 1.1-1.8 Å, 1.8-2.6 Å and more significant than 2.6 Å, from

327   the outside to the centre. A similar pattern was detected in MK (Fig. 6d). Four diffuse rings were

328   detected; 1.1-1.3 Å, 1.3-1.7 Å, 1.7-2.7 Å, and greater than 2.7 Å, which were in concordance with the

329   rings detected in K350-120. The difference is that the intensity between 1.7 and 1.3 Å in MK is much

330   lower than in K350-120. These rings correspond to the amorphous phase in the material and are

331   correlated with the amorphous halos detected through XRD (Trusilewicz et al., 2012). Some crystalline

332   quartz particles (not shown) were detected in all the samples with their characteristic diffraction

333   pattern.
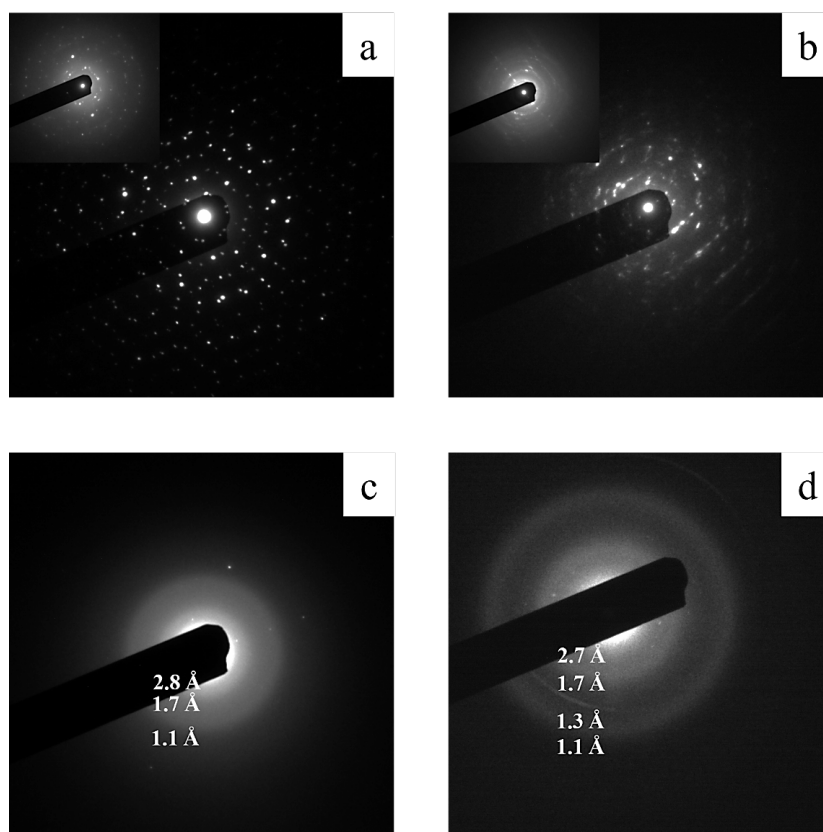
Fig. 6. Representative SAED patterns of (a) K, (b) K250-30, (c) K350-120, and (d) MK.

3.2 OH groups alterations

IR spectra focusing on the 3800-3000 cm^{-1} and 1800-1500 cm^{-1} regions are presented in Fig. 7. The stretching of -OH bonds and the H-O-H bending can be examined in the first and second regions, respectively. The unit cell of kaolinite contains 4 OH groups; hence at least four stretching modes are detected in kaolin IR spectra (Balan et al., 2005). 3620 cm^{-1} band is related to the stretching of the OH groups between tetrahedral and octahedral sheets (inner hydroxyl groups). In contrast, the other three bands correspond to the OH groups at the octahedral sheet's surface (inner-surface hydroxyl groups), which are also weakly bonded with the oxygens from tetrahedral sheets through hydrogen bonds (Madejová, 2003). More concretely, 3650 cm^{-1} and 3670 cm^{-1} bands are related to out-of-phase stretching vibrations of inner-surface OH groups, while ~3695 cm^{-1} band is related to in-phase symmetric stretching of inner-surface OH groups (Hoch and Bandara, 2005; Vaculíková et al., 2011). After the MA, the intensity of the characteristic kaolinite bands decreased, with a slight displacement

348   to higher wavenumbers. Moreover, an extensive centred broad band appeared at around 3300 cm^{-1},

349   confirming that the OH groups' bonding to the kaolinite and illite structures was profoundly modified.

350   This band comprehends the new vibrations of OH in the material in the form of weakly-bonded OH

351   and H_2O (adsorbed or coordinated), probably formed through the reaction between hydroxyl groups

352   (Souri et al., 2015; Johnston, 2017). The newly formed band at ~1635 cm^{-1} assigned to the H-O-H

353   bending mode supports the formation of water (Schuttlefield et al., 2007; Johnston, 2017). In K250-

354   30, all the bands of inner and inner-surface hydroxyls were still detected, despite a significant decrease

355   of the bands corresponding to out-of-phase OH groups stretching. Therefore, the kaolinite structure

356   could be classified as poorly ordered kaolinite (Vaculíková et al., 2011), suggesting that low-energetic

357   mechanical treatments affect the hydroxyls from kaolinite and not many Al-O and Si-O bonds that

358   were observed almost unaltered in previous studies (Mañosa et al., 2022). A least activated sample

359   (K250-15) was also studied for comparison purposes, presenting the same modifications as K250-30

360   but with less reduction of the kaolinite bands. However, here the bands corresponding to the out-of-

361   phase OH stretchings were more discernible, therefore, the kaolinite is more ordered than in K250-30.

362   Increasing the MA, these bands tended to disappear as the kaolinite structure collapsed into amorphous

363   material until being undiscernible in K350-120. As expected, MK did not present bands in this region

364   since the hydroxyls had been eliminated through dehydroxylation.

365
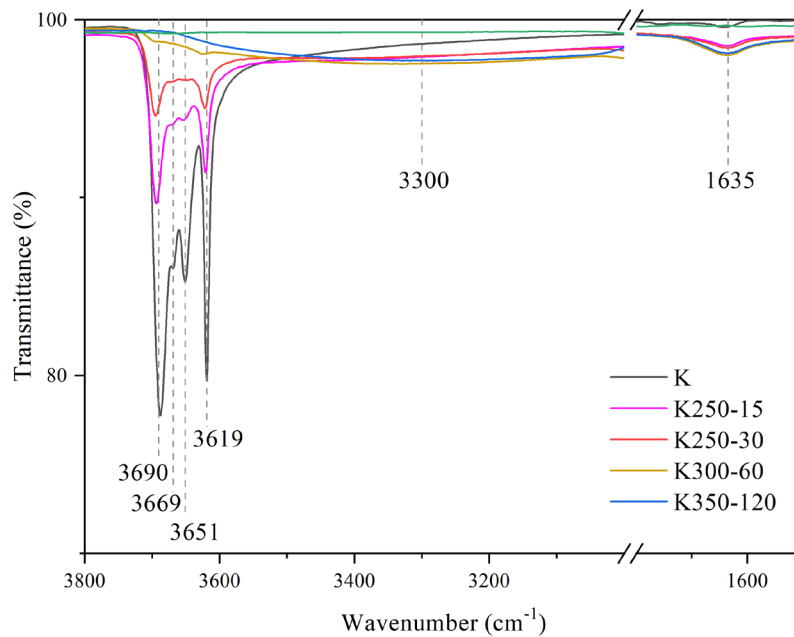
Fig. 7. FTIR spectra of K, K250-15, K250-30, K300-60, K350-120, and MK at the ranges 3800-3000 cm^{-1} and 1800-1500 cm^{-1}.

The modifications of the hydroxyls induced through MA in the kaolinite structure were also supported by TGA and derivative thermogravimetry (DTG). Fig. 8 presents the TGA (solid line) and DTG (dashed line) curves for K, MK and 4 representative samples of MA. Kaolinite presented a dehydroxylation step (~400-700 ºC) where the hydroxyl groups are removed from the structure and released as water vapour. The dehydroxylation in K was detected as a well-defined mass loss in the TGA curve, with its corresponding peak in the DTG, with the maximum at 518 ºC. A shoulder could also be appreciated in this peak, maybe due to the overlapping with illite dehydroxylation, which takes place at temperatures around 550 ºC to 780 ºC, usually with DTG peaks around 700-750 ºC (Sánchez-Soto et al., 2007; Húlan et al., 2017; Wang et al., 2017). After the dehydroxylation, the material is entirely amorphous (metakaolinite) until the transition to mullite at around 1000 ºC, observed at the heat flow signal (not shown), without mass loss associated (De Aza et al., 2014; Kassa et al., 2022). MK did not present mass loss since it was previously calcinated at 750 ºC. Therefore, the hydroxyl groups from kaolinite and illite were removed. However, the MA differs from TA as the OH groups are not removed but separated from the kaolinite structure. With lower grinding, K250-15, the

dehydroxylation step is still the main source of mass loss in the material, with some previous mass loss

due to the release of some weakly bonded hydroxyls. However, the results suggest that very few OHs

were not attached to the structure. The temperature of the dehydroxylation stage in the DTG curve was

also reduced to lower temperatures. In K250-30 there was still an important mass loss through

dehydroxylation, but smaller than in K250-15, since a large part of the hydroxyls were still attached

to the kaolinite structure, as previously suggested in Fig. 7. In contrast, in K300-60, the

dehydroxylation step was minimum, as almost all the kaolinite was transformed. As previously stated

in the text, in K350-120, the kaolinite was fully transformed into amorphous material (metakaolinite).

Hence, the dehydroxylation step was not detected. The TGA curve for this sample was a gradual mass

loss through the range 30-700 ºC approximately, instead of separated steps as in K. The other MA

samples presented an intermediate behaviour due to their different kaolinite contents: a gradual mass

loss at the initial temperatures due to the free OH and H_2O and later a sudden change due to

dehydroxylation of the remaining kaolinite. Focusing on the DTG curve, the maximum of the

dehydroxylation peak was shifted to lower temperatures with increasing mechanical treatment energy.

The peak area was significantly reduced since there was a reduction in the number of structural

hydroxyls and, therefore, less mass loss associated with the dehydroxylation stage (Vizcayno et al.,

2010). This shift is associated with the breakage of hydrogen bonds between kaolinite sheets and the

increased disorder in the structure, causing a weaker bonding force of the hydroxyls (Souri et al.,

2015). A new peak of increasing intensity with MA raised with the maximum at temperatures between

100 ºC and 200 ºC. This peak corresponds to the mass loss of non-bonded OH and newly formed H_2O,

either adsorbed or weakly bonded. The DTG peak is broad due to the presence of differently

configurated water molecules that are more or less strongly bonded to the material's amorphous

structure and therefore released at higher or lower temperatures (Horváth et al., 2003). The appearance

of this new peak supports the hypothesis that the hydroxyls released from the structure react to form

406 water molecules. The total mass loss of the MA samples is higher than K, mainly because the activated
407 samples adsorb atmospheric water which is released at low temperatures (Souri et al., 2015).
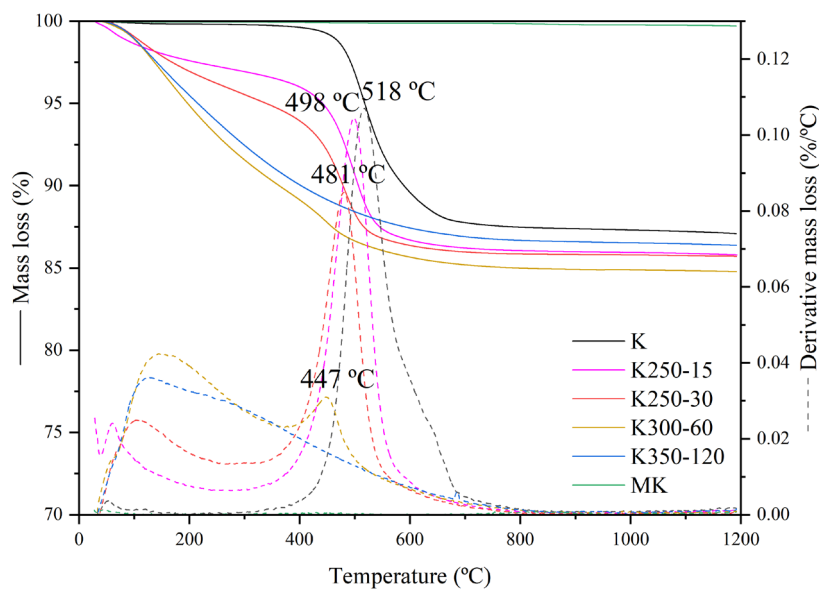

408

409 Fig. 8. TGA (solid line) and DTG (dashed line) of K, K250-15, K250-30, K300-60, K350-120, and
410   MK.

411   To confirm the modifications of the kaolinite's hydroxyl groups induced with the MA, ^{1}H MAS

412 NMR was employed, whose spectra are presented in Fig. 9. In K, a peak and a shoulder were detected

413 at the chemical shifts of 1.9 and 2.8 ppm, respectively. The peaks are in similar chemical shifts to

414 kaolin studied elsewhere (Huittinen et al., 2013; Zhu et al., 2016). Inner-surface OHs are only linked

415 to aluminium octahedral sheets, while inner hydroxyls are also bonded to silicon tetrahedral sheets

416 through hydrogen bonds. Inner hydroxyls (not bonded to other chemical groups) present higher

417 electron density around the proton (Zhu et al., 2016). Therefore, the peak at 1.9 ppm was assigned to

418 inner hydroxyls, and the peak at 2.8 ppm was assigned to inner-surface hydroxyls. An additional weak

419 peak was detected at 6.8 ppm, which was attributed to adsorbed water since it is detected at higher

420 chemical shifts (Fafard et al., 2017). With MA, the OH surroundings were highly altered. In K250-30,

421 the spectrum's shape changes due to a significant contribution at higher chemical shifts. This variation

422 was probably due to the loss of bonding from the hydroxyl groups. This phenomenon, together with

the decrease of inner and inner-surface hydroxyls' intensities, confirms that low-energy mechanical treatments mainly affect OHs causing only some disorder in the kaolinite lattice. After a more intense MA (K300-60), the intensities corresponding to the hydroxyls in kaolinite were even smaller than in K250-30 since kaolinite was almost fully amorphized. In contrast, here the contribution to the peak at higher chemical shifts increases, in accordance with the TGA results where the DTG peak shifted to lower temperatures due to the breakage of OH bonds with the kaolinite structure. In K350-120, the spectrum entirely differs from K. The sharp peak comprehending the inner and inner-surface hydroxyls was substituted by a broad band centred at around 5 ppm. The wide band was probably a sum of the contribution of weakly-bonded hydroxyls and water. Adsorbed water appears at higher chemical shifts (Pálková et al., 2021), therefore, the contribution at lower chemical shifts could be attributed to weakly-bonded OH and/or coordinated water. After kaolin calcination, MK presents a mainly flat background due to the dehydroxylation, with probably a small contribution of physically adsorbed water gained over time. These changes confirm that, through mechanical treatment, the hydroxyls in kaolinite undergo an important disordering from ordered and bonded OH groups to non- and weakly-bonded hydroxyls and water. With the combination of FTIR, TGA and ^{1}H MAS-NMR we confirmed the separation of the hydroxyls from the structure, together with the formation of water molecules, contributing also to the amorphization of the material.
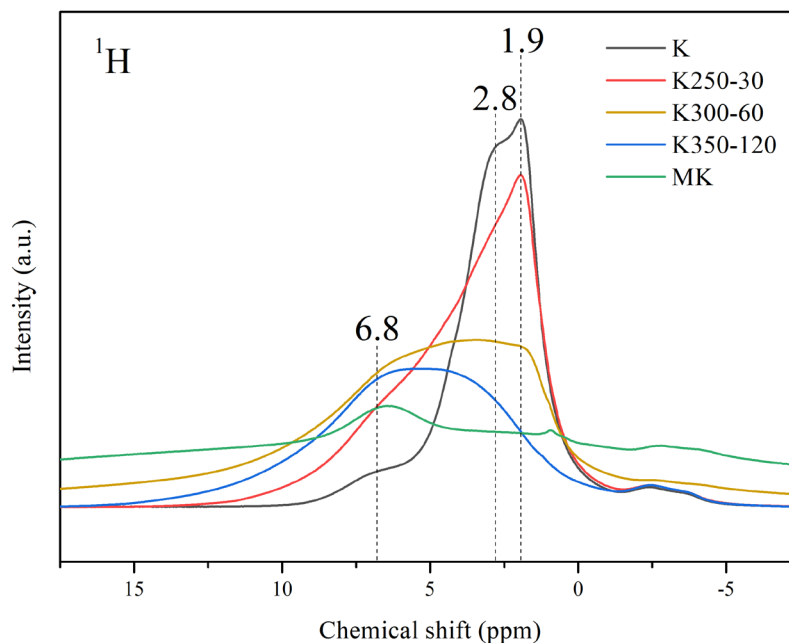
Fig. 9. ^{1}H MAS NMR of K, K250-30, K300-60, K350-120, and MK.

4. Conclusions

This study presented a complete study on the effect of mechanical activation (MA) on kaolinite's (and typical kaolin impurities) structures, which complements a previous study of the reactivity of mechanically activated kaolin (Mañosa et al., 2022). In this work, a synergistic combination of novel techniques was used to enhance the knowledge of the variations in the structure and the hydroxyls' environment of kaolin. Raw kaolin and metakaolin were also used throughout this work as reference materials. The research's main conclusions are the following:

- The evolution of the crystalline phases of the material into amorphous material was monitored through X-ray diffraction (XRD) and transmission electron microscopy (TEM) with selective area electron diffraction (SAED). The initial kaolinite was transformed into amorphous material with various degrees of amorphisation depending on the intensity of the mechanical treatment.

- With the profile fitting of the XRD data, the effect of MA on kaolinite, illite, K-feldspar and quartz was monitored. Both TOPAS and Python pseudo-Voigt fittings presented similar area and width values and the same trends for the mechanically activated samples, confirming the robustness of the study. A great reduction of kaolinite and illite was observed even at the lowest mechanical treatments, while K-feldspar was also significantly reduced at milling with energetic parameters. The crystallite size of all the crystalline phases was also reduced with MA.

- Scanning electron microscopy and TEM confirmed the change in the morphology of the particles through MA, in contrast with thermal activation, where the morphology is practically unchanged.

- The results of thermogravimetry analysis (TGA), Fourier-transform infrared spectroscopy (FTIR) and ^{1}H magic angle spinning nuclear magnetic resonance (MAS NMR) demonstrated that the surroundings of the OH are easily modified with mechanical treatments (even with the less energetic). The structurally bonded hydroxyls are gradually removed from the kaolinite structure, losing the dehydroxylation step detected in TGA and the bands in FTIR. Furthermore, some hydroxyls react to form water molecules that could be free or bonded to the structure.

This work's results contribute to improving the comprehension of mechanically activated kaolin. Furthermore, new characterisation techniques were presented to evaluate the effect of MA on the material and the degree of activation, which could be also used to assess other mechanically activated clays. Future research on the topic could be oriented toward applying the same methodologies to kaolin with different kaolinite contents to evaluate the effect of various impurities on the final material.

References

Balan, E., Lazzeri, M., Saitta, A.M., Allard, T., Fuchs, Y., Mauri, F., 2005. First-principles study of OH-stretching modes in kaolinite, dickite, and nacrite. Am. Mineral. 90, 50–60. https://doi.org/10.2138/am.2005.1675

Baláž, P., Achimovicová, M., Baláž, M., Billik, P., Zara, C.Z., Criado, J.M., Delogu, F., Dutková, E., Gaffet, E., Gotor, F.J., Kumar, R., Mitov, I., Rojac, T., Senna, M., Streletskii, A., Krystyna, W.C., 2013. Hallmarks of mechanochemistry: From nanoparticles to technology. Chem. Soc. Rev. 42, 7571–7637. https://doi.org/10.1039/c3cs35468g

Balczár, I., Korim, T., Kovács, A., Makó, E., 2016. Mechanochemical and thermal activation of kaolin for manufacturing geopolymer mortars – Comparative study. Ceram. Int. 42, 15367–15375. https://doi.org/10.1016/j.ceramint.2016.06.182

Cao, Y., Wang, Y., Zhang, Z., Ma, Y., Wang, H., 2021. Recent progress of utilization of activated kaolinitic clay in cementitious construction materials. Compos. Part B Eng. 211, 108636.

503   https://doi.org/10.1016/j.compositesb.2021.108636

504   De Aza, A.H., Turrillas, X., Rodriguez, M.A., Duran, T., Pena, P., 2014. Time-resolved powder

505   neutron diffraction study of the phase transformation sequence of kaolinite to mullite. J. Eur.

506   Ceram. Soc. 34, 1409–1421. https://doi.org/10.1016/j.jeurceramsoc.2013.10.034

507   De Souza Santos, H., Campos, T.W., De Souza Santos, P., Kiyohara, P.K., 2005. Thermal phase

508   sequences in gibbsite/kaolinite clay: Electron microscopy studies. Ceram. Int. 31, 1077–1084.

509   https://doi.org/10.1016/j.ceramint.2004.10.018

510   Derouiche, R., Baklouti, S., 2021. Phosphoric acid based geopolymerization: Effect of the

511   mechanochemical and the thermal activation of the kaolin. Ceram. Int. 47, 13446–13456.

512   https://doi.org/10.1016/j.ceramint.2021.01.203

513   Efavi, J., Damoah, L., Yaw Bensah, D., Dodoo Arhin, D., Tetteh, D., 2012. Development of porous

514   ceramic bodies from kaolin deposits for industrial applications. Appl. Clay Sci. 65–66, 31–36.

515   https://doi.org/10.1016/j.clay.2012.04.010

516   Fafard, J., Terskikh, V., Detellier, C., 2017. Solid-state ^{1}H and ^{27}Al NMR studies of DMSO-kaolinite

517   intercalates. Clays Clay Miner. 65, 206–219. https://doi.org/10.1346/CCMN.2017.064060

518   Fitos, M., Badogiannis, E.G., Tsivilis, S.G., Perraki, M., 2015. Pozzolanic activity of thermally and

519   mechanically treated kaolins of hydrothermal origin. Appl. Clay Sci. 116–117, 182–192.

520   https://doi.org/10.1016/j.clay.2015.08.028

521   Frost, R.L., Makó, É., Kristóf, J., Horváth, E., Kloprogge, J.T., 2001. Mechanochemical treatment of

522   kaolinite. J. Colloid Interface Sci. 239, 458–466. https://doi.org/10.1006/jcis.2001.7591

523   Georgopoulos, G., Badogiannis, E., Tsivilis, S., Perraki, M., 2021. Thermally and mechanically

524   treated Greek palygorskite clay as a pozzolanic material. Appl. Clay Sci. 215, 106306.

525   https://doi.org/10.1016/j.clay.2021.106306

526   Gobindlal, K., Zujovic, Z., Yadav, P., Sperry, J., Weber, C.C., 2021. The Mechanism of Surface-

527   Radical Generation and Amorphization of Crystalline Quartz Sand upon Mechanochemical

528   Grinding. J. Phys. Chem. C 125, 20877–20886. https://doi.org/10.1021/acs.jpcc.1c06069

529   Hamzaoui, R., Muslim, F., Guessasma, S., Bennabi, A., Guillin, J., 2015. Structural and thermal

530   behavior of proclay kaolinite using high energy ball milling process. Powder Technol. 271,

531   228–237. https://doi.org/10.1016/j.powtec.2014.11.018

Hoch, M., Bandara, A., 2005. Determination of the adsorption process of tributyltin (TBT) and monobutyltin (MBT) onto kaolinite surface using Fourier transform infrared (FTIR) spectroscopy. Colloids Surfaces A Physicochem. Eng. Asp. 253, 117–124. https://doi.org/10.1016/j.colsurfa.2004.10.118

Horváth, E., Frost, R.L., Makó, É., Kristóf, J., Cseh, T., 2003. Thermal treatment of mechanochemically activated kaolinite. Thermochim. Acta 404, 227–234. https://doi.org/10.1016/S0040-6031(03)00184-9

Huittinen, N., Sarv, P., Lehto, J., 2013. A ^{1}H and ^{27}Al NMR investigation of yttrium(III) and europium(III) interaction with kaolinite. Appl. Clay Sci. 80–81, 182–188. https://doi.org/10.1016/j.clay.2013.04.005

Húlan, T., Trník, A., Medveď, I., 2017. Kinetics of thermal expansion of illite-based ceramics in the dehydroxylation region during heating. J. Therm. Anal. Calorim. 127, 291–298. https://doi.org/10.1007/s10973-016-5873-0

Izadifar, M., Thissen, P., Steudel, A., Kleeberg, R., Kaufhold, S., Kaltenbach, J., Schuhmann, R., Dehn, F., Emmerich, K., 2020. Comprehensive Examination of Dehydroxylation of Kaolinite, Disordered Kaolinite, and Dickite: Experimental Studies and Density Functional Theory. Clays Clay Miner. 68, 319–333. https://doi.org/10.1007/s42860-020-00082-w

Johnston, C.T., 2017. Infrared Studies of Clay Mineral-Water Interactions, in: Developments in Clay Science. Elsevier Ltd., pp. 288–309. https://doi.org/10.1016/B978-0-08-100355-8.00009-6

Johnston, C.T., Kogel, J.E., Bish, D.L., Kogure, T., Murray, H.H., 2008. Low-temperature FTIR study of kaolin-group minerals. Clays Clay Miner. 56, 470–485. https://doi.org/10.1346/CCMN.2008.0560408

Kása, E., Baán, K., Kása, Z., Kónya, Z., Kukovecz, Á., Pálinkó, I., Sipos, P., Szabados, M., 2022. The effect of mechanical and thermal treatments on the dissolution kinetics of kaolinite in alkaline sodium aluminate solution under conditions typical to Bayer desilication. Appl. Clay Sci. 229, 106671. https://doi.org/10.1016/j.clay.2022.106671

Kása, E., Szabados, M., Baán, K., Kónya, Z., Kukovecz, Á., Kutus, B., Pálinkó, I., Sipos, P., 2021. The dissolution kinetics of raw and mechanochemically treated kaolinites in industrial spent liquor – The effect of the physico-chemical properties of the solids. Appl. Clay Sci. 203. https://doi.org/10.1016/j.clay.2021.105994

562 Kassa, A.E., Shibeshi, N.T., Tizazu, B.Z., 2022. Kinetic analysis of dehydroxylation of Ethiopian
563   kaolinite during calcination. J. Therm. Anal. Calorim. https://doi.org/10.1007/s10973-022-
564   11452-y

565 Khalifa, A.Z., Cizer, Ö., Pontikes, Y., Heath, A., Patureau, P., Bernal, S.A., Marsh, A.T.M., 2020.
566   Advances in alkali-activation of clay minerals. Cem. Concr. Res. 132, 106050.
567   https://doi.org/10.1016/j.cemconres.2020.106050

568 Madejová, J., 2003. FTIR techniques in clay mineral studies. Vib. Spectrosc. 31, 1–10.
569   https://doi.org/10.1016/S0924-2031(02)00065-6

570 Maier, M., Beuntner, N., Thienel, K.C., 2021. Mineralogical characterization and reactivity test of
571   common clays suitable as supplementary cementitious material. Appl. Clay Sci. 202, 105990.
572   https://doi.org/10.1016/j.clay.2021.105990

573 Makó, É., Frost, R.L., Kristóf, J., Horváth, E., 2001. The effect of quartz content on the
574   mechanochemical activation of kaolinite. J. Colloid Interface Sci. 244, 359–364.
575   https://doi.org/10.1006/jcis.2001.7953

576 Mañosa, J., Cerezo-Piñas, M., Maldonado-Alameda, A., Formosa, J., Giro-Paloma, J., Rosell, J.R.,
577   Chimenos, J.M., 2021. Water treatment sludge as precursor in non-dehydroxylated kaolin-based
578   alkali-activated cements. Appl. Clay Sci. 204. https://doi.org/10.1016/j.clay.2021.106032

579 Mañosa, J., Gómez-Carrera, A.M., Svobodova-Sedlackova, A., Maldonado-Alameda, A., Fernández-
580   Jiménez, A., Chimenos, J.M., 2022. Potential reactivity assessment of mechanically activated
581   kaolin as alternative cement precursor. Appl. Clay Sci. 228.
582   https://doi.org/10.1016/j.clay.2022.106648

583 Marinoni, N., Broekmans, M.A.T.M., 2013. Microstructure of selected aggregate quartz by XRD,
584   and a critical review of the crystallinity index. Cem. Concr. Res. 54, 215–225.
585   https://doi.org/10.1016/j.cemconres.2013.08.007

586 Miranda-Trevino, J.C., Coles, C.A., 2003. Kaolinite properties, structure and influence of metal
587   retention on pH. Appl. Clay Sci. 23, 133–139. https://doi.org/10.1016/S0169-1317(03)00095-4

588 N'Guessan, N.E., Joussein, E., Courtin-Nomade, A., Paineau, E., Soubrand, M., Grauby, O., Robin,
589   V., Cristina, C.D., Vantelon, D., Launois, P., Fondanèche, P., Rossignol, S., Texier-Mandoki,
590   N., Bourbon, X., 2021. Role of cations on the dissolution mechanism of kaolinite in high

591   alkaline media. Appl. Clay Sci. 205. https://doi.org/10.1016/j.clay.2021.106037

592   Osornio-Rubio, N.R., Torres-Ochoa, J.A., Palma-Tirado, M.L., Jiménez-Islas, H., Rosas-Cedillo, R.,

593   Fierro-Gonzalez, J.C., Martínez-González, G.M., 2016. Study of the dehydroxylation of

594   kaolinite and alunite from a Mexican clay with DRIFTS-MS. Clay Miner. 51, 55–68.

595   https://doi.org/10.1180/claymin.2016.051.1.05

596   Pálková, H., Barlog, M., Madejová, J., Hronský, V., Petra, L., Šimon, E., Billik, P., Zimowska, M.,

597   2021. Structural changes in smectites subjected to mechanochemical activation: The effect of

598   the occupancy of the octahedral sites. Appl. Clay Sci. 213.

599   https://doi.org/10.1016/j.clay.2021.106214

600   Peng, H., Vaughan, J., Vogrin, J., 2018. The effect of thermal activation of kaolinite on its

601   dissolution and re-precipitation as zeolites in alkaline aluminate solution. Appl. Clay Sci. 157,

602   189–197. https://doi.org/10.1016/j.clay.2018.03.002

603   Ptáček, P., Frajkorová, F., Šoukal, F., Opravil, T., 2014. Kinetics and mechanism of three stages of

604   thermal transformation of kaolinite to metakaolinite. Powder Technol. 264, 439–445.

605   https://doi.org/10.1016/j.powtec.2014.05.047

606   Richard, D., Rendtorff, N.M., 2022. Kaolin group minerals under pressure: The study of their

607   structural and electronic properties by DFT methods. Appl. Clay Sci. 219, 106444.

608   https://doi.org/10.1016/j.clay.2022.106444

609   Rudmin, M., Banerjee, S., Yakich, T., Tabakaev, R., Ibraeva, K., Buyakov, A., Soktoev, B., Ruban,

610   A., 2020. Formulation of a slow-release fertilizer by mechanical activation of

611   smectite/glauconite and urea mixtures. Appl. Clay Sci. 196, 105775.

612   https://doi.org/10.1016/j.clay.2020.105775

613   San Cristóbal, A.G., Castelló, R., Martín Luengo, M.A., Vizcayno, C., 2010. Zeolites prepared from

614   calcined and mechanically modified kaolins. A comparative study. Appl. Clay Sci. 49, 239–246.

615   https://doi.org/10.1016/j.clay.2010.05.012

616   Sánchez-Soto, P.J., Ruiz-Conde, A., Bono, R., Raigón, M., Garzón, E., 2007. Thermal evolution of a

617   slate. J. Therm. Anal. Calorim. 90, 133–141. https://doi.org/10.1007/s10973-007-7751-2

618   Schuttlefield, J.D., Cox, D., Grassian, V.H., 2007. An investigation of water uptake on clays

619   minerals using ATR-FTIR spectroscopy coupled with quartz crystal microbalance

620   measurements. J. Geophys. Res. Atmos. 112, 1–14. https://doi.org/10.1029/2007JD008973

621   Souri, A., Kazemi-Kamyab, H., Snellings, R., Naghizadeh, R., Golestani-Fard, F., Scrivener, K.,
622   2015. Pozzolanic activity of mechanochemically and thermally activated kaolins in cement.
623   Cem. Concr. Res. 77, 47–59. https://doi.org/10.1016/j.cemconres.2015.04.017

624   Sperinck, S., Raiteri, P., Marks, N., Wright, K., 2011. Dehydroxylation of kaolinite to metakaolin - A
625   molecular dynamics study. J. Mater. Chem. 21, 2118–2125. https://doi.org/10.1039/c0jm01748e

626   Tole, I., Habermehl-Cwirzen, K., Rajczakowska, M., Cwirzen, A., 2018. Activation of a raw clay by
627   mechanochemical process-effects of various parameters on the process efficiency and
628   cementitious properties. Materials (Basel). 11, 6–8. https://doi.org/10.3390/ma11101860

629   Trusilewicz, L., Fernández-Martínez, F., Rahhal, V., Talero, R., 2012. TEM and SAED
630   characterization of metakaolin. Pozzolanic activity. J. Am. Ceram. Soc. 95, 2989–2996.
631   https://doi.org/10.1111/j.1551-2916.2012.05325.x

632   Vaculíková, L., Plevová Eva, Vallová Silvie, Koutnik Ivan, 2011. Characterization and
633   differentiation of kaolinites from selected Czech deposits using infrared spectroscopy and
634   differential thermal analysis. Acta Geodyn. Geomater. 8, 59–67.

635   Valášková, M., Barabaszová, K., Hundáková, M., Ritz, M., Plevová, E., 2011. Effects of brief
636   milling and acid treatment on two ordered and disordered kaolinite structures. Appl. Clay Sci.
637   54, 70–76. https://doi.org/10.1016/j.clay.2011.07.014

638   Vizcayno, C., de Gutiérrez, R.M., Castello, R., Rodriguez, E., Guerrero, C.E., 2010. Pozzolan
639   obtained by mechanochemical and thermal treatments of kaolin. Appl. Clay Sci. 49, 405–413.
640   https://doi.org/10.1016/j.clay.2009.09.008

641   Wang, G., Wang, H., Zhang, N., 2017. In situ high temperature X-ray diffraction study of illite.
642   Appl. Clay Sci. 146, 254–263. https://doi.org/10.1016/j.clay.2017.06.006

643   Wang, H., Li, C., Peng, Z., Zhang, S., 2011. Characterization and thermal behavior of kaolin. J.
644   Therm. Anal. Calorim. 105, 157–160. https://doi.org/10.1007/s10973-011-1385-0

645   Xu, H., Van Deventer, J.S.J., 2002. Microstructural characterisation of geopolymers synthesised
646   from kaolinite/stilbite mixtures using XRD, MAS-NMR, SEM/EDX, TEM/EDX, and HREM.
647   Cem. Concr. Res. 32, 1705–1716. https://doi.org/10.1016/S0008-8846(02)00859-1

648   Zhao, B., Liu, L., Cheng, H., 2021. Rational design of kaolinite-based photocatalytic materials for

649   environment decontamination. Appl. Clay Sci. 208, 106098.

650   https://doi.org/10.1016/j.clay.2021.106098

651   Zhu, X., Zhu, Z., Lei, X., Yan, C., 2016. Defects in structure as the sources of the surface charges of

652   kaolinite. Appl. Clay Sci. 124–125, 127–136. https://doi.org/10.1016/j.clay.2016.01.033

653